High-performance bimetallic Ni-Mn Phosphate hybridized with 3-D graphene foam for novel hybrid supercapacitors

Abdulmajid A. Mirghni, Kabir O. Oyedotun, Oladepo Fasakin, Badr A. Mahmoud, Delvina Japhet Tarimo and Ncholu Manyala*

Department of Physics, Institute of Applied Materials, SARChI Chair in Carbon Technology and Materials, University of Pretoria, Pretoria 0028, South Africa.

*Corresponding author's email: ncholu.manyala@up.ac.za, Tel.: + (27)12 420 3549

Abstract

Nickel-manganese phosphate/graphene foam (GF) composite was successfully synthesized through a simple and direct hydrothermal approach, serving as highly efficient electrodes for hybrid device. Ni and Mn are both redox metals owing to their multiple oxidation states however, Ni-based materials possess higher capacity due to its strong faradic mechanism while Mn-based materials offer pseducapacitive nature and GF for its ability to improve the surface area as well as the electrical conductivity of the composite. Consequently, the prepared $NiMn(PO_4)_2$/GF composite achieved a maximum specific capacity of 97 mAh g^{-1} at 0.5 A g^{-1} in a 3-electrode configuration setup compared to 63 mAh g^{-1} for the pristine material. Thus, $NiMn(PO_4)_2$/GF considered as a positive electrode in a hybrid device with carbon derived from Capsicum (bell pepper) seeds "peppered"-activated carbon (ppAC) as a negative electrode. The hybrid device reported a maximum energy density of 35.42 Wh kg^{-1} corresponding to a power density of 538 W kg^{-1} at 0.5 A g^{-1}. The $NiMn(PO_4)_2$/GF//ppAC hybrid device also showed high stability of 97.8% capacity retention over 10000 cycles at 6 A g^{-1}, ~93% float time efficiency after 120 hours and could still preserve ~1.17 V against its initial cell potential of 1.5 V after 60 hours of self-discharge. The outstanding performance of $NiMn(PO_4)_2$/GF material in a half and full cell makes it a good candidate for supercapacitor application.

Keywords: Hybrid device; Metal phosphate; Supercapacitor; Energy storage; Graphene, Composite

1. Introduction

The global concern of sustainable energy issues falls under two prospectives: Energy generation and energy-storage. Solar, wind, and hydropower among others are always renewable energy sources. A satisfied use of these renewable sources requires highly effective energy storing devices [1][2]. Fuel cells, batteries and electrochemical capacitors are considered to be a crucial topics for researchers in the field of energy storage devices [3][4][5]. The challenges are to use capable electrode materials, electrolytes, and separators to assemble highly efficient storage devices.

Metal phosphates (MPs) are widely established as promising candidate materials for supercapacitor due to their lower resistivity, charge storage capacity, and open structure with different morphologies [6]. For instance, Zining Wang et al. synthesized $NiHPO_4$ nanowires on nickel foam using a one-step hydrothermal method, and they reported a specific capacitance of 1472 F g^{-1} at 1 A g^{-1}, even though the materials showed a clear Faradic behavior in which a specific capacity (Cg^{-1} or mAh g^{-1}) should have been reported. The material, coupled in a device with AC delivered a specific capacitance of 98.62 F g^{-1} at 0.5 A g^{-1}, energy density of 26.8 Wh kg^{-1} and power density of 68.8 W kg^{-1} [7]. Bo Yan and co-workers used GO to coat $MnPO_4.H_2O$ prepared with one-step hydrothermal method, they also claimed a specific capacitance of 287.9 F g^{-1} at 0.625 A g^{-1} in 3 M KOH. The material was used to build symmetric device, and produced a maximum energy density of 5.78 Wh kg^{-1} and power density of $1.5x10^5$ W kg^{-1} [8].

The work done using MPs as electrodes for supercapacitors mainly focuses on single MPs, which means not many studies have been reported on bi-MPs for better understanding of these materials. A successful way of enhancing the performance of single metallic material is to combine two transitional metals to form a bimetallic electrode material. This will result in the synergistic effect of both metals that will improve the conductivity and electrochemical performance of the composite [9]. Arthi Gopalakrishman and co-workers synthesized NiCoP by thermal decomposition method with controlled hollow nano-spheres. Then, the NiCoP material was incorporated with carbon nanofibers to form freestanding NiCoP-CNFs through electrospinning, which exhibited a specific capacitance of 200 F g^{-1} at 0.17 A g^{-1}. The authors

assembled NiCoP-CNFs in a hybrid device with AC, which delivered an energy density of 10.7 Wh kg^{-1}, a power density of 137.519 W kg^{-1} and capacitance retention of 88.5% for 5000 cycles in 6 M KOH [10]. Meilin Liu et al. fabricated $NaNi_xCo_{1-x}PO_4 \cdot H_2O$ following microwave method, reported a specific capacitance of 828 F g^{-1} at 1 A g^{-1} in 1 M KOH. The authors designed an asymmetric device based on graphene (G) as a negative electrode and $NaNi_xCo_{1-x}PO_4 \cdot H_2O$ as a positive electrode, operated in a cell potential of 1.5 V, obtained a maximum energy density of 29.85 Wh kg^{-1} and equivalent power density of 374.95 W kg^{-1} at 1 A g^{-1}. The asymmetric device also exhibited a capacitance retention of 76.9% for over 10000 cycles [11].

Regardless of the work done on MPs as promising electrodes for energy storage however, a deep understanding of these materials is still lacking. Driving by the research curiosity on the synthesis and electrode hybridizing of MPs herein, we have reported nickel manganese bimetallic phosphate facilitated with graphene foam electrodes for hybrid supercapacitor device via a hydrothermal method. Synergizing nickel with manganese in the presence of GF known for its high specific surface area and moderate pore size distribution [6][12][36][38], as conductivity facilitator is believed to strongly boost the electrochemical performance of the material based on: (1) Ni-based materials possess higher capacity due to its strong faradic mechanism [12], (2) Mn-based materials offer pseducapacitive nature [13], and (3) GF can improve the surface area as well as the electrical conductivity of the composite. Graphene, like other carbon materials such as activated carbon (AC) and carbon nanotube (CNT), exhibits electrical double-layer (EDLC) charge storage mechanism, where charges are physically stored by electrostatic charge adsorption at the interface between the electrode and electrolyte. One of the significant features of the EDLC is that no charge transfer occurs between the interface of electrode and electrolyte. The advantages of graphene as electrode for energy storage is the high conductivity associated with the sheet like lends itself to rapid transport electrons to and from the active materials sites. Besides, the mechanical strength of the graphene has the potential to absorb some of the expansion and contraction of the anchored nanoparticles during the intercalation and de-intercalation processes, which typically lead to mechanical failure of the electrode and performance reduction through the loss of intimate contact of the active material and the conductive carbon black mixed into the electrode material for enhanced conductivity

[14][33][36]. Moreover, both Ni and Mn are globally obtainable at low-cost, meeting the need for naturally abundant electrodes for practical applications. The hybridized $NiMn(PO_4)_2$/GF supplied an enhanced specific capacity of 97 mAh g^{-1} at 0.5 A g^{-1}. Therefore, $NiMn(PO_4)_2$/GF considered as a positive electrode in a hybrid device with carbon derived from Capsicum (bell pepper) seeds "peppered"-activated carbon (ppAC) as a negative electrode, delivered an energy density of 35.42 Wh kg^{-1} corresponding to a power density of 538 W kg^{-1} at 0.5 A g^{-1}. The $NiMn(PO_4)_2$/GF//ppAC showed a high stability of 97.8% capacity retention over 10000 cycles at 6 A g^{-1}.

2. Synthesis of $NiMn(PO_4)_2$ and $NiMn(PO_4)_2$/GF composite

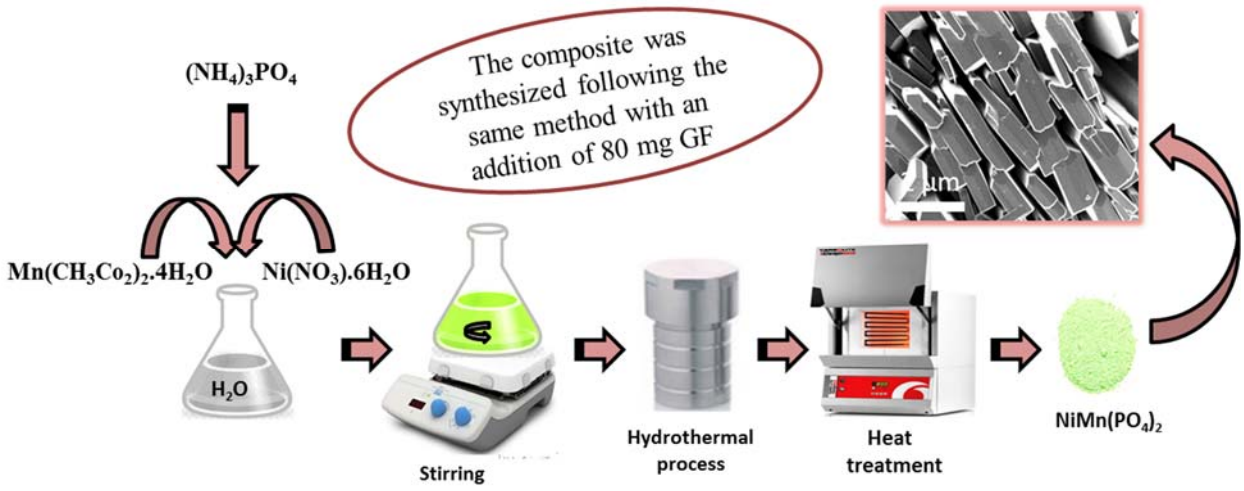

Scheme 1: Synthesis of $NiMn(PO_4)_2$ and $NiMn(PO_4)_2$/GF composite

Stoichiometric amount based on molecular weight for $Ni(NO_3)_2.6H_2O$, $Mn(CH_3Co)_2.4H_2O$ and $(NH_4)PO_4$ were mixed in 20 ml DI water each. The solutions were mixed together and stirred for 30 min. The mixture was then transferred into Teflon-lined, stainless-steel autoclave for hydrothermal reaction at temperature 120° C, and dwelling of time 3 hours in an eclectic oven. The sample was removed, filtered, and washed repeatedly with DI water and placed in an atmospheric oven at 60° C for 12 hours for complete drying. The recovery product was verified as $NiMn(PO_4)_2$ (see Scheme 1: synthesis diagram). For the synthesis of $NiMn(PO_4)_2$/GF, first GF

was synthesized through CVD system detailed in reference [15]. The same process mentioned in Scheme 1 was used to synthesize $NiMn(PO_4)_2$/GF composite, with 80 mg of graphene foam (GF) being introduced in the first mixing step of precursors. An optimization process was carried out in which the composite with 80 mg graphene foam was observed as material with optimum mass of GF owing to its better electrochemical performances as compared to those with 20 mg, 40 mg and 100 mg of GF, respectively (see Figure S3 in the supporting information).

3. Synthesis of activated carbon from pepper seed waste (ppAC)

Waste pepper seeds were collected and washed several times before drying. The dried seeds were then grinded and mixed with activating agent ($KHCO_3$) in an agate mortar at different mass ratios of 1:0.5, 1:1 and 1:2, respectively. Deionized water was added to the mixture to make a mold, which was dried overnight in an oven at 80^o C to remove the water thereafter, placed in a tubular furnace and gradually heated to 850^o C at a ramp rate of 5^o C min^{-1}. The system was left for 2 h under 250 sccm of Argon gas flow with the volume of Argon gas flow reduced by half after 1.5 h and the sample was left to naturally cool to room temperature. This was done to create extra porosity in the material through gasification within the reaction chamber. The product was sonicated and washed with 3 M HCl for 12 h to remove impurities and unreacted inorganic salts (if any). Thereafter, further rinsing with deionized water was performed until a neutral pH was obtained. The final product was then dried at 80^o C to obtain Capsicum-activated carbons labelled as ppAC.

4. Structure, morphology, and electrochemical characterization of the prepared materials

The structure and crystal status of the materials were studied using a Bruker BV 2D Phaser Benchtop X-ray diffraction (XRD) instrument with reflection geometry at 2ϑ values (10–90°) with a 5.240 s requisition time per step, operating with a Cu $K\alpha_1$ radiation source (λ = 0.15406 nm) at 50 kV and 30 mA. A WITec Confocal Raman Microscope (WITec alpha 300 R, Germany), Laser

wavelength 532 nm, laser power 4 mW and spectral acquisition time 120-s was used for Raman analysis. The scanning electron micrograph (SEM) images were obtained from a Zeiss Ultra plus 55 field emission scanning electron microscope (FE-SEM) (Carl Zeiss, Oberkochen, Germany) operated at accelerating voltage of 2.0 kV. Transmission electron microscopy (TEM) analysis was measured at 200 kV on a JEOL JEM-2100F microscope with field-emission gun. The samples were sonicated for 30 minutes in an ethanol then the uniform dispersion dropped onto the copper grid for analysis. To fabricate electrodes for 3-electrode configuration, 80% of the active material was mixed together with 10% polyvinylidene difluoride (PVDF) as a binder and 10% of carbon black (to compensate for reduction in conductivity of the active material, which emanated from the addition of binder (PVDF)). A 1-methyl-2- pyrrolidinone (NMP) solvent was later added to make slurry. The homogenously mixed slurry was pasted on the nickel foam (1 cm^2 diameter) and allocated in an electric oven at 60 ^oC for 12 hours to completely evaporate NMP. The mass of each of the single electrodes was about 3 mg/cm^2. The electrochemical measurements were explored in a 3-electrode system using 1 M KOH aqueous electrolyte, the active material as working electrode, Ag/AgCl (3M KCl saturated) as reference electrode and glassy carbon as counter electrode. A coin cell type CR2025 was used to assemble the hybrid device. $NiMn(PO_4)_2$/GF and ppAC were used as positive and negative electrodes respectively and the microfiber glass filter paper was used to separate the two electrodes. Cyclic voltammetry (CV) and galvanostatic charge-discharge (GCD) were performed to ascertain the storage mechanism in the device. Both the CV and GCD were carried out in a cell potential ranging between 0.0 and 1.5 V. The impedance of the hybrid device was also investigated with electrochemical impedance spectroscopy (EIS) in range 100 kHz to 0.01 Hz with zero potential amplitude using a Bio-logic VMP-300 potentiostat (Knoxville, US) driven by the EC-lab software.

The specific capacity (mAh g^{-1}) based on the charge stored was calculated from the GCD curve using the following formula:

$$C_s = \frac{Q}{3.6} \quad \text{..... (1)}$$

Where $Q=I\Delta t$ is the charge, consequently I (A) is the specific current and Δt(s) is the discharge time

Since the electrochemical performance of positive electrode ($NiMn(PO_4)_2$/GF) and negative electrode (ppAC) are different depending on their charge storage mechanism, the charge quantities in these electrodes were balanced as per the formulae (2) and (3).

$q_+ = q_-$ ..... (2)

Equation (2) can be expressed as a function of specific capacity for the positive electrode and specific capacitance for the negative electrode as follow [37]:

$$m_+ q_{s+} = m_- \Delta V_- C_{S-} \Rightarrow \frac{m_-}{m_+} = \frac{q_{S+}}{\Delta V_- C_{S-}} \quad \text{..... (3)}$$

Where q_+ and q_- represent negative and positive charges respectively, m_+ and m_- represent the active masses of the positive and negative electrodes, respectively, ΔV is the potential window of the negative electrode (ppAC), C_S is specific capacitance of the negative electrode (ppAC) and *qs* represents the specific charge (charge per mass) of the positive electrode. The mass ratio of the positive and negative electrodes (m_+:m_-) based on charge stored for both materials was calculated from formula (3) as 1:2.25 respectively, translating to 1.6 and 3.6 mg for positive and negative electrodes respectively with total device mass of 5.2 mg/cm^2. Two important parameters for evaluating the device; energy density E_d *(Wh kg^{-1})* and power density P_d *(W kg^{-1})* were calculated based on the total weight of the active materials (positive and negative) from GCD curves using formula (4) and (5):

$$E_d = \frac{i}{3.6m}\int V dt \quad \text{..... (4)}$$

$$P_d = 3600\frac{E_d}{\Delta t} \quad \text{..... (5)}$$

Where *i* represents applied current (mA), *m* represents the total mass of the active material (mg), $\int Vdt$ represents the area under discharge curve of the device, and *Δt* is the discharge time (s)

5. Results and discussion

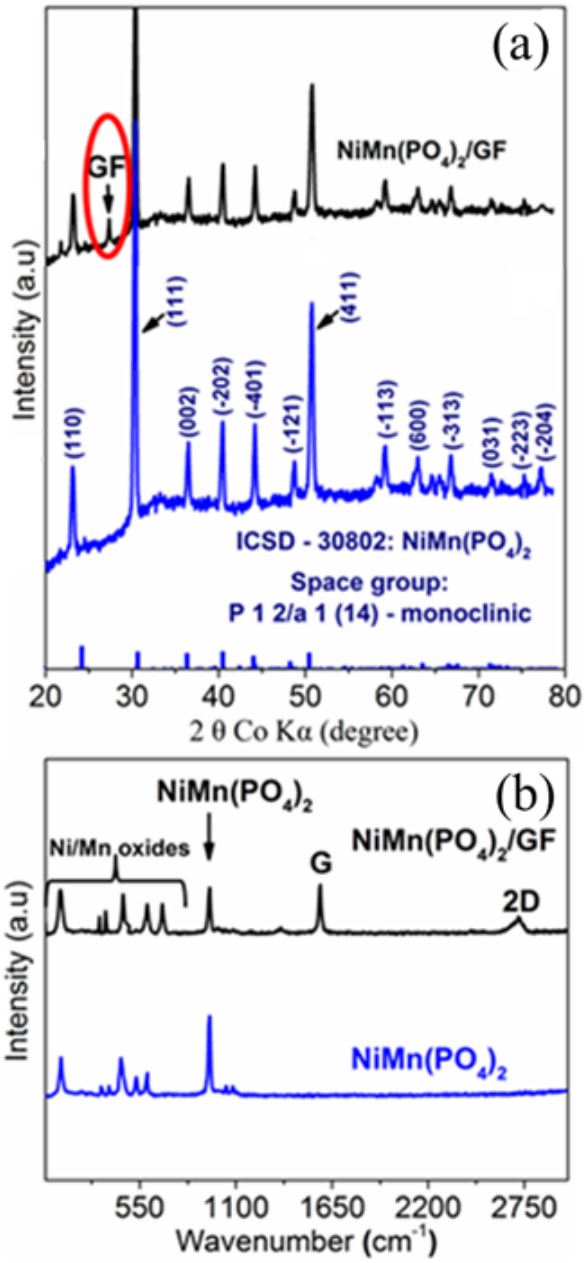

Figure 1: XRD patterns of (a) pristine $NiMn(PO_4)_2$ (ICSD No. 30802) together with $NiMn(PO_4)_2$/GF composite, and (b) Raman spectra of $NiMn(PO_4)_2$ and $NiMn(PO_4)_2$/GF.

Figure 1 (a) shows XRD pattern of the pristine $NiMn(PO_4)_2$ with that of $NiMn(PO_4)_2$/GF composite measured at 2θ range between 20°−80°. Visualization Molecular Structure Diamond Crystal (VMSD) software was used to study the structural analysis of the materials. The XRD pattern indicates the characteristic peaks of pure $NiMn(PO_4)_2$ phase and all the visible peaks can be referred to pure monoclinic phase, space group: P 1 2/a 1 (14), cell parameter: a=10.267, b=4.726, c=5.961, a/b=2.1725, b/c=0.7928, c/a=0.5806, cell volume= 289.21 Å. This phase is in accordance with ICSD-30802. The highly intense peaks of XRD pattern with predominant (111) diffraction peak at ~30.3° confirming the high crystallinity state of the material. It can be observed from the figure that the XRD patterns of $NiMn(PO_4)_2$ and $NiMn(PO_4)_2$/GF are similar however, an additional peak of (002) at about 27.2° observed and identified to be carbon peak as a result of the presence of GF in the $NiMn(PO_4)_2$/GF composite [16]. Figure 1(b) shows Raman spectra of $NiMn(PO_4)_2$ and $NiMn(PO_4)_3$/GF composite. In the spectra of $NiMn(PO_4)_2$, the peaks at ~530 and 595 cm^{-1} are ascribed to stretching modes of Ni−O, while bending modes of O−Mn−O appeared at ~ 329 and 373 cm^{-1} [17][18]. The bending modes O−P−O are observed at ~ 440 cm^{-1}. The strong modes at ~ 954 cm^{-1} are assigned to symmetric stretching vibrations of O−P−O [19], and the external modes are identified at ~97. All these modes confirm the formation of $NiMn(PO_4)_2$. In the spectra of $NiMn(PO_4)_2$/GF, an additional G and 2D peaks at ~ 1580 and 2717 $cm^{-}1$ were observed respectively, these G and 2D bands are descriptive of C–C vibration mode and double resonance process respectively [20].

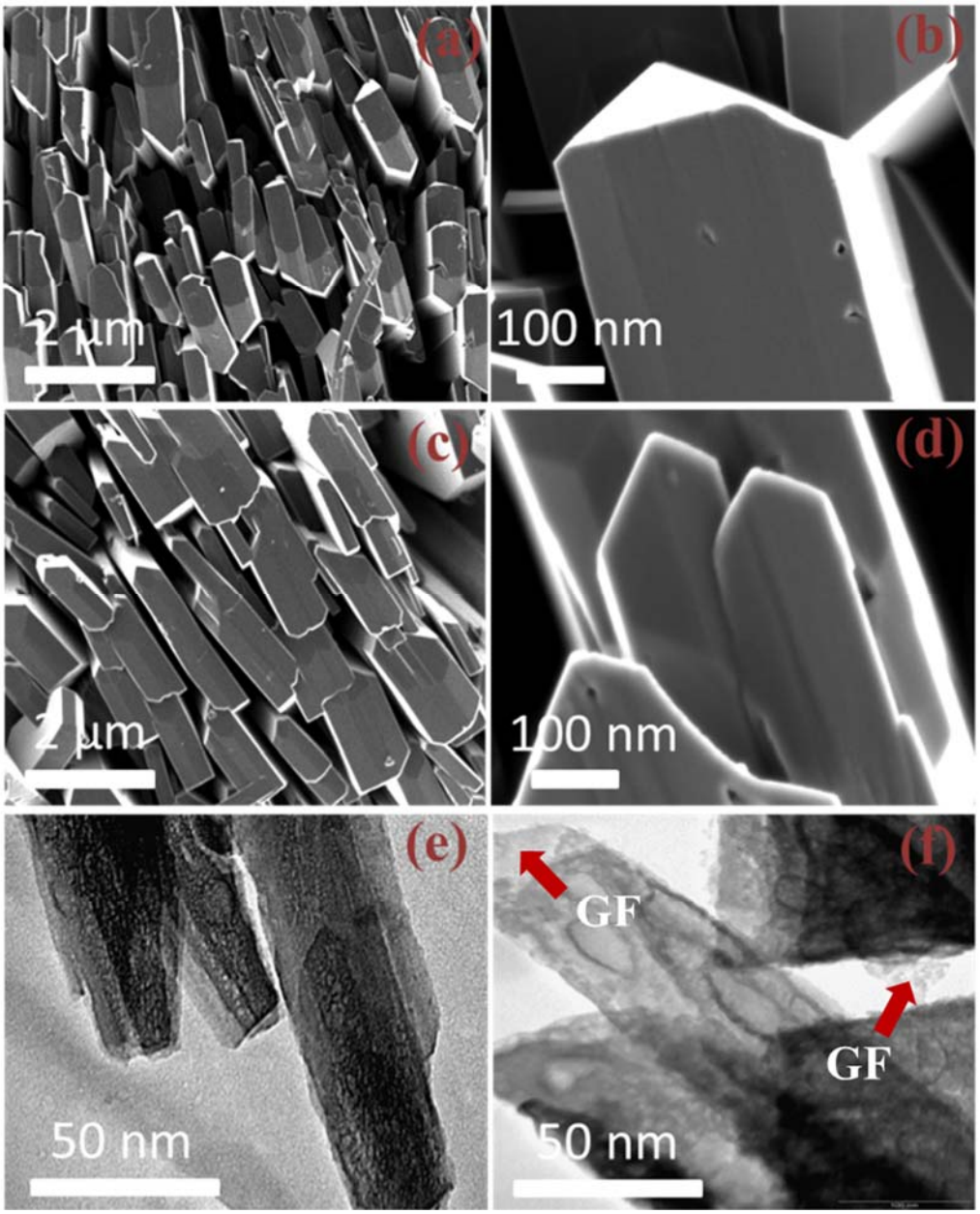

Figure 2: (a & b) Low and high magnification SEM images of $NiMn(PO_4)_2$, (c & d) Low and high magnification of SEM images of $NiMn(PO_4)_2$/GF and (e & f) TEM images of $NiMn(PO_4)_2$ and $NiMn(PO_4)_2$/GF respectively.

Figure 2 presents SEM and TEM micrographs which show the morphology of $NiMn(PO_4)_2$ as well as $NiMn(PO_4)_2$/GF composite. In Figure 2(a, b), the $NiMs(PO_4)_2$ material shows cubic rods

morphology with orderly building block appearance. From SEM images in figure 2(c, d) the cubic rods are looking more ordered which could be as a result of the presence of GF in the composite. Nevertheless, the presence of GF is not visible in SEM images, but could be observed in XRD pattern as well as Raman spectrum (see Figure 1(b, c)). The SEM could only generate a variety of signals, resulting from interactions of the electron beam with atoms at or near the surface of the materials thus, not capable of showing the underlying GF layers. [15]. Figure 2(e, f) represents TEM micrographs of $NiMn(PO_4)_2$ and $NiMn(PO_4)_2$/GF composite, respectively, measured at 50 nm. The materials reveal cubic rods in agreement with the observed SEM images in Figure 2(a, b, c and d). In figure 2(f), the GF could be seen together with $NiMn(PO_4)_2$ material owing to the TEM higher penetrating power compared to that of SEM. The GF layers revealed by the TEM indicate the successful incorporation of GF in the composite material. The dispersal of GF within the $NiMn(PO_4)_2$ materials is highly desired to offer the required surface for effective charge storage process [21].

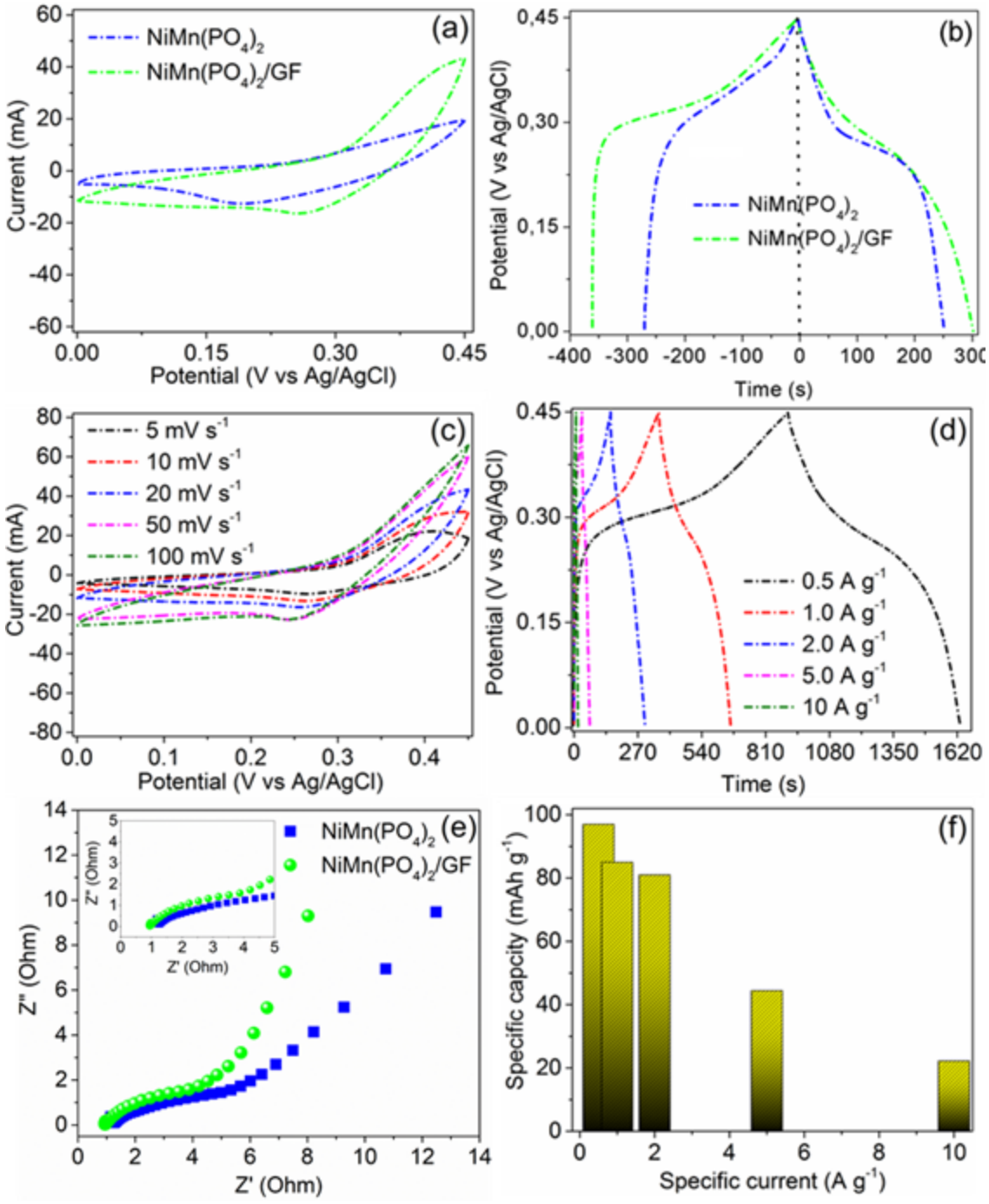

Figure 3: (a) CV curves comparing $NiMn(PO_4)_2$ and $NiMn(PO_4)_2$/GF at 20 mV s^{-1}, (b) GCD curves comparing $NiMn(PO_4)_2$ and $NiMn(PO_4)_2$/GF at 1 A g^{-1}, (c) CV curves of $NiMn(PO_4)_2$/GF at different scan rates, (d) GCD curves of $NiMn(PO_4)_2$/GF at different specific currents, (e) Nyquist plot of $NiMn(PO_4)_2$ and $NiMn(PO_4)_2$/GF and (f) Specific capacity calculated for $NiMn(PO_4)_2$/GF at different specific currents.

The electrochemistry part of the materials was carried out using a CV, GCD and EIS in half cell as well as in full cell. The CV and GCD curves in Figure 3 (half cell) were tested in a potential window range 0.0 to 0.45V, while the EIS tested in a range of 100 kHz to 0.01 Hz. Figure 3(a) compares the CV curves of $NiMn(PO_4)_2$ and $NiMn(PO_4)_2$/GF at a scan rate of 20 mV s^{-1}. Interestingly $NiMn(PO_4)_2$/GF possesses a higher current response due to an impact of the GF present in the composite. The convenient explanation of this is, the GF incorporated in $NiMn(PO_4)_2$ has improved the specific surface area as well as the conductivity of the composite. This is due to the fact that graphene decreases resistance of the host material and boosts the charge collection ability of $NiMn(PO_4)_2$/GF material, as a result, eases the movement of ions within the electrode [22]. This flexible and fast movement is required for energy storage mechanism. Figure 3(b) also compares the GCD curves of $NiMn(PO_4)_2$ and $NiMn(PO_4)_2$/GF at a specific current of 1 A g^{-1}. The curves agree with CVs in Figure 3(a) as $NiMn(PO_4)_2$/GF is having a longer discharge time compared to $NiMn(PO_4)_2$. Figure 3(c) displays CVs of $NiMn(PO_4)_2$/GF at scan rates of 5, 10, 20, 50 and 100 mV s^{-1}. In this figure, the material exhibits a pseuducapacitive mechanism, which implies that the material stores the energy in a redox reaction [23]. A pair of broad peaks was seen at about 0.24 V and 0.39 V respectively, these peaks might be due to the electron transfer between Ni^{2+} and Ni^{3+} ($Ni^{2+} \leftrightarrow Ni^{3+}$) and also Mn^{2+} and Mn^{3+} ($Mn^{2+} \leftrightarrow Mn^{3+}$) [24][25]. The observed redox reactions arise from the active elements of Ni^{2+}/Ni^{3+} and in Mn^{2+}/Mn^{3+} in the NiMn precursor or $NiMn(PO_4)_2$ at the interface between the electrode and electrolyte is as follow: $NiMn(PO_4)_2 + OH^- \leftrightarrow NiMn(OH)(PO_4)_2 + e^-$ and $NiMn(PO_4)_2(OH) + OH^- \leftrightarrow NiMn(OH)_2(PO_4)_2 + e^-$. The two states, Ni^{2+}/ Ni^{3+} and Mn^{2+}/Mn^{3+} are mixed in the materials, with both Ni^{2+}/ Ni^{3+} and Mn^{2+}/Mn^{3+} redox couples ensure a major electrocatalytic effectiveness based on the synergistic redox reaction involving the changes in oxidation states with OH^- present in KOH electrolyte [25][35]. In figure 3(c), as the scan rate increases, two observations could be pointed out: (1) The current response increases (due to faster movement of the ions as the scan rate increases) and (2) the CV shapes remain same even at higher scan rate (due to high reversibility of charging and discharging processes). Figure 3(d) presents GCD curves of $NiMn(PO_4)_2$/GF at specific currents of 0.5, 1, 2, 5, and 10 A g^{-1}. As expected, the curves show a pseuducapacitive mechanism consistent with CV in figure 3(c). The Nyquist plot of the $NiMn(PO_4)_2$ and $NiMn(PO_4)_2$/GF also showed in Figure 3(e), the equivalent

series resistance (ESR) for both samples $NiMn(PO_4)_2$ and $NiMn(PO_4)_2$/GF estimated from intercept to the Z'-axis are 0.82 Ω and 1.2 Ω, respectively. The charge transfer resistance (R_{CT}) was also calculated for $NiMn(PO_4)_2$ and $NiMn(PO_4)_2$/GF by considering the semicircle in the Nyquist plot as 4.18 Ω and 5.21 respectively. The smaller ESR and R_{CT} values calculated for $NiMn(PO_4)_2$/GF compared to $NiMn(PO_4)_2$ are due to the existence of GF in the composite which resulted in a better electrochemical performance of the composite. The bar chart in Figure 3(f) shows the values of specific capacities calculated for $NiMn(PO_4)_2$/GF at specific currents of 0.5, 1, 2, 5 and 10 A g^{-1}. The maximum specific capacity calculated at specific currents of 0.5, 1, 2, 5 and 10 A g^{-1} are 97, 85, 81, 44.4 and 22.2 mAh g^{-1} respectively. These high specific capacity values are referred to as hybridizing of both bimetallic Ni and Mn, for the fact that Ni offers high capacity depending on its rich faradic reaction, while Mn offers less capacity but also pseudocapacitive intent [26]. Secondly, the synergy between $NiMn(PO_4)_2$ and GF facilitates the flexible movements of the ions in and out of the material.

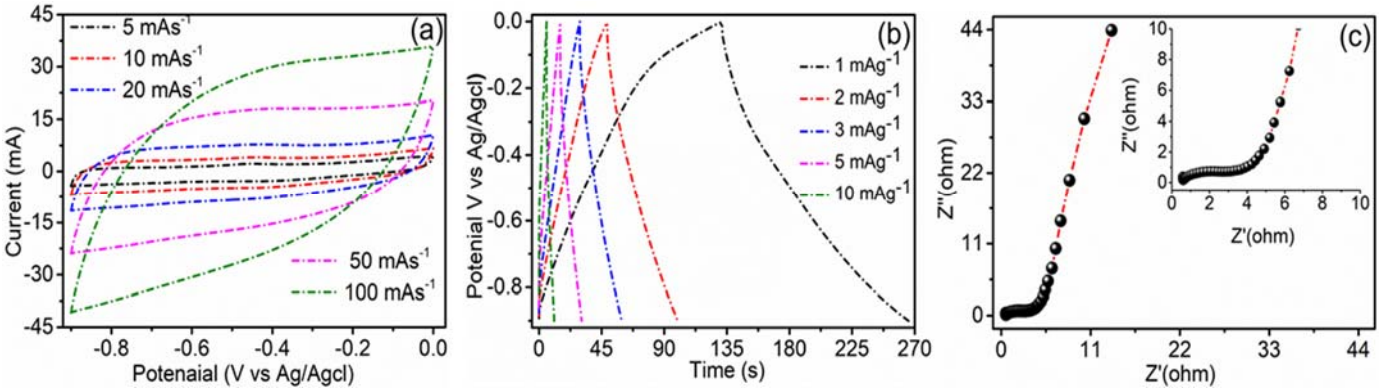

Figure 4: (a,b &c) CV, GCD and EIS of ppAC measured in 3-electrode setup.

Figure 4 displays the electrochemistry properties of the carbon derived from Capsicum (bell pepper) seeds "peppered"-activated carbon (ppAC) used as negative electrode in the fabricated hybrid device. Figure 4(a) shows the CV curve of the ppAC material in the potential range of -0.9 V to 0.0 V. The current response was observed to consistently increase as the scan rates increase from5 mV s^{-1} to 100 mV s^{-1}, indicating a high reversibility rate, which is one of the major strengths of carbon-based materials. The displayed CV curves in figure 4(a) are consistent with the

perceived GCD curves in figure 4(b) as both CVs and GCDs are revealing EDLC mechanism. Figure 4(c) shows the Nyquist EIS plot of the negative ppAC electrode material, revealing an ESR and R_{CT} values of 0.43 Ω and 3.4 Ω, respectively. The diffusion path length for the material is short and close to the ideal vertical line, indicating its good electrochemical behavior. The low values of ESR and R_{CT} recorded for the ppAC material indicate a high electrical conductivity and good capacitive properties [27][28]. Such material is expected to synergize well with the as-synthesized $NiMn(PO_4)_2$/GF for fabrication of high performance hybrid device since the $NiMn(PO_4)_2$/GF composite material could offer high specific capacity. The synthesis method and full characterization of the "peppered"-activated carbon (ppAC) used as a negative electrode in the hybrid device were already reported in our previous work [29].

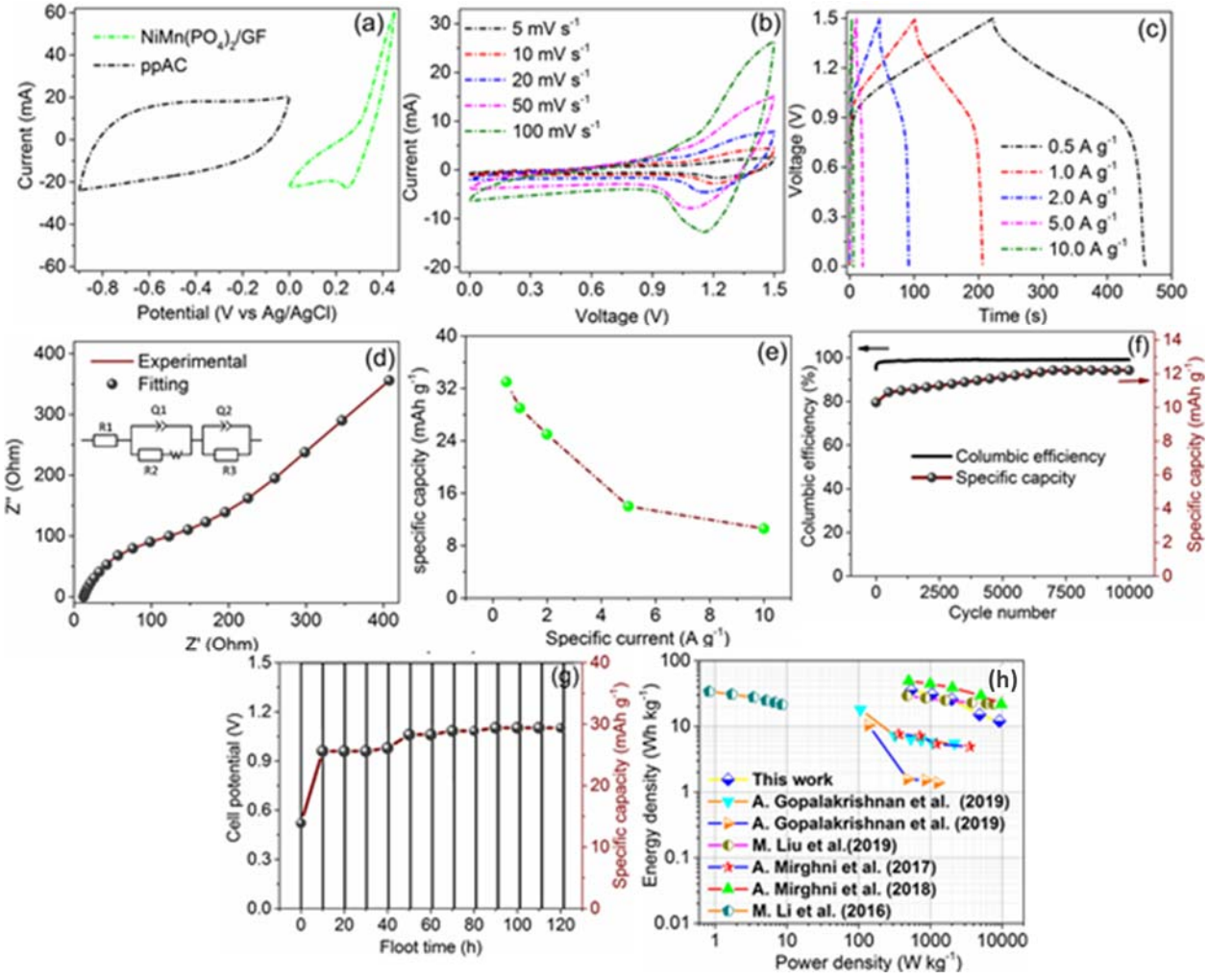

Figure 5: (a) CV curves of $NiMn(PO_4)_2$/GF and ppAC tested in 3-electrode setup, (b & c) CV and GCD of $NiMn(PO_4)_2$/AC hybrid device, (d) Nyquist plot of the $NiMn(PO_4)_2$/AC hybrid device (the inset is equivalent circuit used to fit the EIS data of the device), (e) specific capacity of the hybrid device calculated at different specific currents, (f) double Y plot displaying columbic efficiency and specific capacity versus cycle number at 6 A g^{-1} of the hybrid device, (g) double Y plot displaying cell potential and specific capacity versus float time, (h) Ragone plot of $NiMn(PO_4)_2$/AC hybrid device compared with other similar devices reported in the literature.

In order to further investigate the capability of $NiMn(PO_4)_2$/GF in a hybrid supercapacitor, a full cell supercapacitor ($NiMn(PO_4)_2$/GF//ppAC) was established based on $NiMn(PO_4)_2$/GF as a positive electrode and activated carbon from pepper seed as a negative electrode. Figure 5(a) represents CVs of $NiMn(PO_4)_2$/GF and ppAc tested in 3-electrode setup. The $NiMn(PO_4)_2$/GF was tested in 1M KOH within a potential range of 0.0 to 0.45 V as stated earlier, while ppAC was also tested in 1M KOH within a potential range of -0.9 to 0.0 V. Both materials are performing differently based on their potential, current response and mechanism, therefore, charge balance was verified by considering equations (2) and (3). Figure 5(b) shows CVs of $NiMn(PO_4)_2$/GF//ppAC hybrid device at scan rates of 5, 10, 20, 50 and 100 mV s^{-1} in a cell potential range of 0.0 to 1.5 V. The CVs of the hybrid device in Figure 5(b) can be discussed in two points: (1) The curves display an electric double layer (EDLC) performance in the range 0.0 to 0.9 V, which is a reflection of the presence of EDLC mechanism arisen from ppAC, (2) they also display a faradic performance in the range of 0.9 to 1.5, which is a reflection of oxidation and reduction mechanism resultant from reversible redox reaction of $Ni^{2+} \leftrightarrow Ni^{3+}$ and $Mn^{2+} \leftrightarrow Mn^{3+}$. However, as far as the full range CV curve is concerned, the hybrid device gives a faradic signature. Figure 5(c) represents GCDs of the $NiMn(PO_4)_2$/GF//ppAC hybrid device in a cell potential range 0.0 to 1.5 V. From physical inspection, the GCDs are showing a faradic appearance in the full cell potential which means they agree well with the noticed CVs in Figure 5(b). Since the CVs and GCDs in Figure 5(b, c) showed a faradic performance, specific capacities (mAh g^{-1}) at different specific currents were calculated as shown in Figure 5(e) [30]. The hybrid device possessed specific capacity values of 33, 29, 26, 14 and 8.3 mAh g^{-1} at specific currents of 0.5, 1, 2, 5, and 10 A g^{-1} respectively.

The impedance parameters of the hybrid device were obtained from the Nyquist plot in figure 5(d). The intercept to the Z' axis in the high-frequency region indicates the equivalent series resistance (ESR), which is a summation of the electrolyte's ionic resistance, the intrinsic resistance of the electrode material, the contact resistance of electrode/current collector interface as well as the electrode/electrolyte interface. The R_{CT} usually caused by charge transfer process on the surface of the electrode. The inset to figure 5(d) represents the circuit used to fit the experimental data and one can see that there is such a good agreement with the experimental data. In the circuit diagram, the equivalent series resistance (ESR) denoted as R1, is in series with charge transfer resistant (R_{CT}) denoted as R2 and the Warburg diffusion element (W) which is in parallel with real capacitance Q1 [31]. The mass capacitance (Q2) was detected in the low-frequency region as the line tends to be vertical; however, a deviation from the ideal vertical performance was caused by the leakage resistance (R_L) [32].

The stability of the hybrid device was investigated in the form of charge–discharge cycling, floating time and self-discharge. Figure 5(f) displays a double Y plot of the specific capacity and columbic efficiency against the cycle number for a long-term cycling of 10000 cycles at 6 A g^{-1}. The specific capacity was calculated at an interval of 500 cycles through 10000 cycles. As seen from Figure 5(f), the specific capacity gradually increased until ~7000 cycles then stabilized for the rest number of cycles. This increase occurred because of the full accessibility of the ions into initially inaccessible pores of the material, which takes time for the material to get complete wettability. The hybrid device could preserve 97.8% of its initial capacity. The columbic efficiency of the hybrid device recorded at ~100% over the 10000 cycles. Figure 5(g) shows a progression of $NiMn(PO_4)_2$/GF//ppAC hybrid device over float time of 120 hrs continuously measured at 1 A g^{-1}. The specific capacity was calculated every 10 h for 120 hrs. In the first 10 hrs, the specific capacity increased quickly then stabilized for 30 hrs before slight increased again after 40 hrs. This fluctuating in the values of specific capacity could be due to the wettability process-taking place at the initial cycles. Afterward, the specific capacity interestingly stabilized from 50 hrs at almost the same value until 120 h. This performance which is in agreement with cycling in figure 5(f) is due to the strong and stable structure of the positive material and the synergistic effect between $NiMn(PO_4)_2$ and ppAC on the hybrid device.

Figure 5(h) shows a Ragone plot comparing the energy and power density values of the $NiMn(PO_4)_2$/GF//ppAC hybrid device and other single and bimetallic phosphate-based devices. The maximum energy density value received for the $NiMn(PO_4)_2$/GF//ppAC hybrid device was 35.42 Wh kg^{-1} at 0.5 A g, equivalent to a power density of 538 W kg^{-1}. At a higher specific current of 10 A g^{-1}, the hybrid device delivered a highest power density of 9128 W kg^{-1}, equivalent to the energy density of 9.2 Wh kg^{-1}. Comparing to other single and bimetallic phosphate-based devices, the $NiMn(PO_4)_2$/GF//ppAC hybrid device is assessed to be comparable in performance with some similar materials from the literature as depicted in Figure 5(h). More details about reported phosphate based hybrid devices and this work are shown in table 1 for a better comparison.

Table 1: A comparison data of $NiMn(PO_4)_2$/GF//ppAC hybrid device with other phosphate-based devices

Phosphate based hybrid device	electrolyte	E_d (Wh kg^{-1})	P_d (W kg^{-1})	Stability	Ref
Ni_1Co_9P-CNFs	6 M KOH	17.7	106.7	88.5%: 5000 cycles	[10]
Ni_1Co_9P//AC	6 M KOH	10.7	137.519	86.7%: 5000 cycles	[10]
AC//$Mn_3(PO_4)_2$/GF	6 M KOH	7.6	360	96%: 10000 cycles	[33]
$Ni_3(PO_4)_2$/90 mg GF//C-FP	6 M KOH	49	499	53%: 10000 cycles	[34]
$NaNi_{0.33}Co_{0.67}PO_4{\cdot}H_2O$//G	1 M KOH	29.85	374.95	76.9%: 10000 cycles	[11]
$Ni_3(PO_4)_2$//AC	1 M NaOH	26.75	750	87%: 5000	[24]
$NiMn(PO_4)_2$/GF//ppAC	1 M KOH	35.42	538	90.8%: 10000 cycles	This work

6. Conclusion

To sum up, $NiMn(PO_4)_2$ possessing a crystal structure of monoclinic and morphology of cubic rods was successfully prepared through a hydrothermal approach. The selection of these metals (Ni & Mn) was based on the fact that, Ni and Mn are both redox metals owing to their multiple oxidation states however, Ni-based materials possess higher capacity due to its strong faradic mechanism while Mn-based materials offer pseducapacitive nature. Therefore, having two redox metals in the composite enhances its capacity. Moreover, graphene was exposed into the matrix of the material to further enhance the conductivity and surface texture. As a result, the electrochemical performances of $NiMn(PO_4)_2$/GF were found to be superior to Ni-phosphate [34], Mn-phosphate [6] and pristine $NiMn(PO_4)_2$. The $NiMn(PO_4)_2$/GF received a maximum

specific capacity of 97 mAh g^{-1} at 0.5 A g^{-1}. A hybrid device was assembled by placing $NiMn(PO_4)_2$/GF as a positive electrode and ppAC as a negative electrode of the device, accomplishing maximum energy and power density values of 35.42 Wh kg^{-1} and 538 W kg^{-1} at 0.5 A g^{-1}. The $NiMn(PO_4)_2$/GF//ppAC hybrid device tested in a long term of 10000 cycles stability however, it retained a 97.8% capacity retention at 6 A g^{-1}. The device also subjected to a more reliable stability test of floating time for 120 hours and efficiently reserved 93%. Based on the reported results, $NiMn(PO_4)_2$/GF is considered as a high potential material that can possibly impress the future of energy storage.

Acknowledgements

This work is based on research supported by the South African Research Chairs Initiative (SARChI) of the Department of Science and Technology and the National Research Foundation (NRF) of South Africa (Grant No. 61056). Any opinion, finding and conclusion or recommendation expressed in this material is that of the author(s) and the NRF does not accept any liability in this regard. Abdulmajid A. Mirghni acknowledges the financial support from the University of Pretoria, the NRF through the SARChI in Carbon Technology and Materials, and Al Fashir University, Sudan.

References

[1] H.L. Lord, W. Zhan, J. Pawliszyn, Fundamentals and applications of needle trap devices: Acritical review, Analytica Chimica Acta, 677 (2010) 3-18.

[2] M.R. Lukatskaya, B. Dunn, Y. Gogotsi, Multidimensional materials and device architectures for future hybrid energy storage, Nat. Commun. 7 (2016) 1–13.

[3] P. Simon, Y. Gogotsi, B. Dunn, Where Do Batteries End and Supercapacitors Begin?, Science, 343 (2014) 1210–1211.

[4] M. Forghani, S.W. Donne, Method comparison for deconvoluting capacitive and pseudo-capacitive contributions to electrochemical capacitor electrode behavior, J. Electrochem. Soc.

165 (2018) A664–A673.

[5] M. Beidaghi, Y. Gogotsi, Capacitive energy storage in micro-scale devices: Recent advances in design and fabrication of micro-supercapacitors, Energy Environ. Sci. 7 (2014) 867–884. https://doi.org/10.1039/c3ee43526a.

[6] A.A. Mirghni, M.J. Madito, T.M. Masikhwa, K.O. Oyedotun, A. Bello, N. Manyala, Hydrothermal synthesis of manganese phosphate/graphene foam composite for electrochemical supercapacitor applications, J. Colloid Interface Sci. 494 (2017) 325–337.

[7] Z. Wang, F. Chen, P. Kannan, S. Ji, H. Wang, Nickel phosphate nanowires directly grown on Ni foam as binder-free electrode for pseudocapacitors, Mater. Lett. 257 (2019) 1–4

[8] B. Yan, D. Bin, F. Ren, Z. Xiong, K. Zhang, C. Wang, Y. Du, Facile Synthesis of MnPO4·H2O Nanowire/Graphene Oxide Composite Material and Its Application as Electrode Material for High Performance Supercapacitors, Catalysts. 6 (2016) 1–15.

[9] A.A. Mirghni, K.O. Oyedotun, O. Olaniyan, B.A. Mahmoud, N.F. Sylla, N. Manyala, Electrochemical analysis of Na–Ni bimetallic phosphate electrodes for supercapacitor applications, RSC Adv. 9 (2019) 25012–25021.

[10] A. Gopalakrishnan, D. Yang, J.C. Ince, Y.B. Truong, A. Yu, S. Badhulika, Facile one-pot synthesis of hollow NiCoP nanospheres via thermal decomposition technique and its free-standing carbon composite for supercapacitor application, J. Energy Storage. 25 (2019) 1–12.

[11] M. Liu, N. Shang, X. Zhang, S. Gao, C. Wang, Z. Wang, Microwave synthesis of sodium nickel-cobalt phosphates as high-performance electrode materials for supercapacitors, J. Alloys Compd. 791 (2019) 929–935.

[12] B. Liang, Y. Chen, J. He, C. Chen, W. Liu, Y. He, X. Liu, N. Zhang, V.A.L. Roy, Controllable Fabrication and Tuned Electrochemical Performance of Potassium Co-Ni Phosphate Microplates as Electrodes in Supercapacitors, ACS Appl. Mater. Interfaces. 10 (2018) 3506–3514.

[13] C. Chen, N. Zhang, Y. He, B. Liang, X. Liu, Controllable Fabrication of Amorphous Co □ Ni Pyrophosphates for Tuning Electrochemical Performance in Supercapacitors, ACS Appl. Mater. Interfaces. 8 (2016) 23114–23121.

[14] A.A. Mirghni, K.O. Oyedotun, B.A. Mahmoud, A. Bello, S.C. Ray, N. Manyala, Nickel-cobalt phosphate/graphene foam as enhanced electrode for hybrid supercapacitor, Compos. Part B Eng. 174 (2019) 1–11.

[15] A. A. Khaleed, A. Bello, J. K. Dangbegnon, F. U. Ugbo, F. Barzegar, D. Y. Momodu, M. J. Madito, T. M. Masikhwa, O. Olaniyan, and N. Manyala, A facile hydrothermal reflux synthesis of Ni(OH)2/GF electrode for supercapacitor application, J Mater Sci 51 (2016) 6041–6050.

[16] T.P. Shende, B.A. Bhanvase, A.P. Rathod, D. V. Pinjari, S.H. Sonawane, Sonochemical synthesis of Graphene-Ce-TiO2 and Graphene-Fe-TiO2 ternary hybrid photocatalyst nanocomposite and its application in degradation of crystal violet dye, Ultrason. Sonochem. 41 (2018) 582–589.

[17] M. Baril, H. Assaaoudi, I.S. Butler, Pressure-tuning Raman microspectroscopic study of cobalt(II), manganese(II), zinc(II) and magnesium(II) pyrophosphate dihydrates, J. Mol. Struct. 751 (2005) 168–171.

[18] C. V. Ramana, A. Ait-Salah, S. Utsunomiya, U. Backer, A. Mauger, F. Gendron, C.M. Julien, Structural characteristics of lithium nickel phosphate studied using analytical electron microscopy and raman spectroscopy, Chem. Mater. 18 (2006) 3788–3794.

[19] a C. Chapman, L.E. Thirlwell, The infra-red spectra ot orthophosphates, Spectrochim. Acta. 20 (1964) 937–947.

[20] I. Vlassiouk, S. Smirnov, I. Ivanov, P.F. Fulvio, S. Dai, H. Meyer, M. Chi, D. Hensley, P. Datskos, N. V Lavrik, Electrical and thermal conductivity of low temperature CVD graphene : the effect of disorder, Nanotechnology 22 (2011) 1–9.

[21] B. Zhao, T. Sun, X. Zhou, X. Liu, X. Li, K. Zhou, L. Dong, D. Wei, Three-dimensional graphene composite containing graphene-SiO 2 nanoballs and its potential application in stress sensors, Nanomaterials. 9 (2019) 1–11.

[22] H. Lee, J. Kang, M.S. Cho, J.B. Choi, Y. Lee, MnO2/graphene composite electrodes for supercapacitors: The effect of graphene intercalation on capacitance, J. Mater. Chem. 21 (2011) 18215–18219.

[23] V. Augustyn, P. Simon, B. Dunn, Pseudocapacitive oxide materials for high-rate electrochemical energy storage, Energy Environ. Sci. 7 (2014) 1597–1614.

[24] X. Zhang, J. Li, Y. Sun, Q. Liu, J. Guo, Hybridized Ni(PO3)2-MnPO4 nanosheets array with excellent electrochemical performances for overall water splitting and supercapacitor Xiao, Electrochim. Acta. 299 (2019) 835–843.

[25] B. Senthilkumar, K.V. Sankar, L. Vasylechko, Y.S. Lee, R.K. Selvan, Synthesis and electrochemical performances of maricite-NaMPO 4 (M = Ni, Co, Mn) electrodes for hybrid supercapacitors, RSC Adv. 4 (2014) 53192–53200.

[26] M. Li, J.P. Cheng, J. Wang, F. Liu, X.B. Zhang, The growth of nickel-manganese and cobalt-manganese layered double hydroxides on reduced graphene oxide for supercapacitor, Electrochim. Acta. 206 (2016) 108–115.

[27] K.O. Oyedotun, D.Y. Momodu, M. Naguib, A.A. Mirghni, T.M. Masikhwa, A.A. Khaleed, N. Manyala, Electrochemical performance of two-dimensional Ti 3 C 2 -Mn 3 O 4 nanocomposites and carbonized iron cations for hybrid supercapacitor electrodes, Electrochimica Acta. 301 (2019) 487–499.

[28] K.O. Oyedotun, T.M. Masikhwa, A.A. Mirghni, B.K. Mutuma, N. Manyala, Electrochemical properties of asymmetric supercapacitor based on optimized carbon-based nickel-cobalt-manganese ternary hydroxide and sulphur-doped carbonized iron-polyaniline electrodes, Electrochim. Acta. 334 (2020) 1–12.

[29] D. Momodu, N.F. Sylla, B. Mutuma, A. Bello, T. Masikhwa, S. Lindberg, A. Matic, N. Manyala, Stable ionic-liquid-based symmetric supercapacitors from Capsicum seed-porous carbons, J. Electroanal. Chem. 838 (2019) 119–128.

[30] T.S. Mathis, N. Kurra, X. Wang, D. Pinto, P. Simon, Y. Gogotsi, Energy Storage Data Reporting in Perspective—Guidelines for Interpreting the Performance of Electrochemical Energy Storage Systems, Adv. Energy Mater. 1902007 (2019) 1–13.

[31] W. Sun, X. Chen, Preparation and characterization of polypyrrole films for three-dimensional micro supercapacitor, Journal of Power Sources, 193 (2009) 924–929.

[32] H. Li, J. Wang, Q. Chu, Z. Wang, F. Zhang, S. Wang, Theoretical and experimental specific capacitance of polyaniline in sulfuric acid, Journal of Power Sources, 190 (2009) 578–586.

[33] A.A. Mirghni, M.J. Madito, T.M. Masikhwa, K.O. Oyedotun, A. Bello, N. Manyala, Hydrothermal

synthesis of manganese phosphate/graphene foam composite for electrochemical supercapacitor applications, J. Colloid Interface Sci. 494 (2017) 325-337.

[34] A.A. Mirghni, M.J. Madito, K.O. Oyedotun, T.M. Masikhwa, N.M. Ndiaye, S.J. Ray, N. Manyala, A high energy density asymmetric supercapacitor utilizing a nickel phosphate/graphene foam composite as the cathode and carbonized iron cations adsorbed onto polyaniline as the anode, RSC Adv. 8 (2018) 11608–11621.

[35] K.O. Oyedotun, M.J. Madito, D.Y. Momodu, A.A. Mirghni, T.M. Masikhwa, N. Manyala, Synthesis of ternary NiCo-MnO2 nanocomposite and its application as a novel high energy supercapattery device, Chemical Engineering Journal 335 (2018) 416-433.

[36] K. O. Oyedotun and N. Manyala, Graphene foam–based electrochemical capacitors, Current Opinion in Electrochemistry 21 (2020) 125–131.

[37] A. Noori, M. F. El-Kady, M. S. Rahmanifar, R. B. Kaner and M. F. Mousavi, Towards establishing standard performance metrics for batteries, supercapacitors and beyond, Chem. Soc. Rev. 48 (2019) 1272–1341.

[38] A. Bello, O. O. Fashedemi, J. N. Lekitima, M. Fabiane, D. Dodoo-Arhin, K. I. Ozoemena, Y. Gogotsi, A. T. C. Johnson, and N. Manyala, High-performance symmetric electrochemical capacitor based on graphene foam and nanostructured manganese oxide, AIP Advances 3 (2013) 082118-9.